As-Se pentagonal linkers to induce chirality and polarity in mixed-valent Fe-Se tetrahedral chains resulting in hidden magnetic ordering

Eranga H. Gamage,[a,b] Saeed Kamali,[c,d] Judith K. Clark,[e] Yongbin Lee,[b] Philip Yox,[a,b] Padraic Shafer,[f] Alexander A. Yaroslavtsev,[g] Liqin Ke,[b] Michael Shatruk,[e,h] Kirill Kovnir [a,b,*]

[a] *Department of Chemistry, Iowa State University, Ames, Iowa 50011, USA*

[b] *Ames Laboratory, U.S. Department of Energy, Ames, Iowa 50011, USA*

[c] *Mechanical, Aerospace & Biomedical Engineering Department, University of Tennessee Space Institute, Tullahoma, TN 37388, USA*

[d] *Department of Physics and Astronomy, Middle Tennessee State University, Murfreesboro, TN 37132, USA*

[e] *Department of Chemistry and Biochemistry, Florida State University, Tallahassee, FL 32306, USA*

[j] *Advanced Light Source, Lawrence Berkeley National Laboratory, Berkeley, CA 94720, USA*

[g] *Department of Physics and Astronomy, Uppsala University, Uppsala 75120, Sweden*

[h] *National High Magnetic Field Laboratory, 1800 E Paul Dirac Dr, Tallahassee, FL 32310, USA*

Abstract

A novel mixed-valent hybrid chiral and polar compound, $Fe_7As_3Se_{12}(en)_6(H_2O)$, has been synthesized by a single-step solvothermal method. The crystal structure consists of 1D $[Fe_5Se_9]$ chains connected via $[As_3Se_2]$-Se pentagonal linkers and charge-balancing interstitial $[Fe(en)_3]^{2+}$ complexes (*en* = ethylenediamine). Neutron powder diffraction verified that interstitial water molecules participate in the crystal packing. Magnetic polarizability of the produced compound was confirmed by X-ray magnetic circular dichroism (XMCD) spectroscopy. X-ray absorption spectroscopy (XAS) and ^{57}Fe Mössbauer spectroscopy showed the presence of mixed-valent Fe^{2+}/Fe^{3+} in the Fe-Se chains. Magnetic susceptibility measurements reveal strong AFM nearest neighbor interactions within the chains with no apparent magnetic ordering down to 2 K. Hidden local magnetic ordering below 70 K was found by ^{57}Fe Mössbauer spectroscopy showing that a fraction of the Fe^{3+}/Fe^{2+} atoms in the chains are magnetically ordered. Nevertheless, the magnetic ordering is incomplete even at 6 K. Analysis of XAS spectra demonstrates that the fraction of Fe^{3+} in the chain increases with decreasing temperature. Computational analysis points out several competing ferrimagnetic ordered models within a single chain. This competition, together with variation of the Fe oxidation state and additional weak *intra*chain interactions, are hypothesized to prevent full 3D magnetic ordering.

Introduction

Transition metal based pnictides and arsenides are an interesting class of compounds with exciting magnetic and superconducting properties that have been extensively studied and categorized. The family of 1111 compounds is characterized by negatively charged Fe*Pn* (*Pn*: pnictogen, P and As) and positively charged *Ln*O (*Ln*: lanthanide) layers with high superconducting transition temperatures (T_c).[1,2] In 2008, doping of $BaFe_2As_2$[3–5] with alkali metals was shown to induce superconductivity in $Ba_{0.6}K_{0.4}Fe_2As_2$ with T_c ~ 38 K, introducing a new family of 122 superconductors.[6–8] In the same year, *Jin et al*. synthesized LiFeAs compound belonging to a new family termed 111 superconductors with T_c = 18 K.[9] A simplest 11 family consists of binary iron chalcogenides such as tetragonal Fe*Ch* (*Ch* = Se, T_c = 8 K;[10] *Ch* = S, T_c = 5 K),[11] and Te-doped Fe sulfides and selenides, $FeCh_{1-x}Te_x$.[12] The majority of aforementioned compounds have been synthesized by traditional solid state methods. Only a few attempts have been made to synthesize Fe-based superconductors in solution.[13] A new small bandgap iron sulfide hybrid semiconductor composed of $[Fe_8S_{10}]^{2-}$ puckered layers was synthesized by solvothermal methods using ethylenediamine (*en*) as solvent.[14,15] Variation of the synthetic conditions allowed the excision of 1D $FeSe_2$ chains from FeSe layers due to separation of these chains by positively charged Fe-amine complexes.[16–18] Using a combination of $[Fe(en)_3]^{2+}$ and Cl^- ions to stabilize 1D $FeSe_2$ chains led to the tuning of magnetic properties into spin-glass state.[19] Although the octahedral complexes such as *tris*-$[Fe(en)_3]^{2+}$ are chiral, presence of both Δ- and Λ-isomers in solution makes most of the compounds crystallize in centrosymmetric space groups. An exception to this rule was recently reported for a Co-Se layered hybrid compound.[20] In the current work we hypothesize that chiral low-dimensional Fe-Se fragments can be stabilized using chiral inorganic covalent linkers, such as As-Se rings.

Chiral magnetic materials are known to show short-range hidden ordering and frustrated moments because of the breaking of the inversion symmetry in the crystal field.[21,22] While extensive research has been conducted to synthesize magnetic pnictide-chalcogenide materials in solution, experimental studies on such chiral compounds with magnetic order are rare. Some of the mostly studied chiral compounds include magnetic silicides such as MnSi[23] and $Fe_{1-x}Co_xSi$[24] that exhibit spin helix chirality and skyrmion excitations due to Dzyaloshinskii-Moriya (DM) interactions.[25,26] Ferromagnetic $Nd_2Mo_2O_7$[27] and antiferromagnetic $LiZn_2Mo_3O_8$[28–31] have been widely analyzed for their intriguing magnetic frustration driven by spin chirality. Reports on chiral transition metal chalcogenides are quite uncommon, except for $Cr_{1/3}NbS_2$, which exhibits a helical spin structure due to DM exchange interaction.[32–34] Solution synthesis of magnetic and chiral organic-inorganic hybrids mainly relies on the use of chiral ligands, which, due to weak non-covalent host-framework interactions, may have little impact on the framework structure and properties. Although many compounds with anionic As-Se fragments have been studied, no compound with 1D or 2D Fe-As-Se covalent framework has been reported to the best of our knowledge.

Synthesis of transition metal arsenides in solution is challenging due to difficulties in solubilizing elemental arsenic.[35] However, synthesis of transition metal chalcogenidoarsenates

has been achieved by solution-based approaches.[36–38] A majority of such organic-inorganic hybrid compounds contain arsenic not as a part of the transition metal-chalcogenide framework but as charge-balancing selenoarsenate anions.[39–42] *Sheldrick* and co-workers synthesized a series of manganese selenoarsenate compounds with terpyridine ligands.[43–45] Non-centrosymmetric molecular arsenic selenides such as As_4Se_4 (D_{2d}) and As_4Se_3 (C_{3v}) are more soluble than elemental arsenic. Consequently, they have been used as precursors to synthesize hybrid selenoarsenates.[46–48] *Ansari et al*. reported that dissolution of As_4Se_4 in amine solvents cleaves As-As bonds to form $As_4Se_6^{2-}$ (C_1) and, in the presence of excess polyselenide anions, this ion further fragments resulting in the formation of $As_2Se_6^{2-}$ (C_i) with exocyclic As-Se bonds.[48,49] Reports by *Ibers et al.* showed how $[As_xSe_y]^{z-}$ anions can be extracted from metal arsenic selenides using ammonia and ethylenediamine.[50,51] These anionic motifs can combine with transition metals in solution to form extended structures. Here we report the structure and properties of a unique mixed-valent, antiferromagnetic, chiral and polar compound, $Fe_7As_3Se_{12}(en)_6(H_2O)$ = $[Fe(en)_3]_2[Fe_5Se_9][As_3Se_2]$-$Se(H_2O)$, with pentagonal $[As_3Se_2]$-Se linkers connecting 1D quinto-tetrahedral Fe-Se chains in a 2D layered network. This compound was synthesized using molecular As_4Se_4 precursor in a low temperature solvothermal reaction free of chiral ligands.

Experimental section

Warning

In the solid state reactions performed in sealed silica ampoules at elevated temperatures, arsenic can generate high vapor pressures that can compromise the silica ampoules. Minimum amounts of arsenic (mM scale) should be used in a single ampoule, and the ampoules should be covered with silica wool to contain the shattered glass in case of an explosion. Thermal annealing and opening of ampoules should be performed in a well-ventilated space, preferably in a fume hood.

Synthesis of As_4Se_4

Stoichiometric amounts of arsenic powder (Sigma Aldrich, 99.99%) and selenium powder (-100 mesh, Sigma Aldrich, 99.5%) were weighed in a 1:1 ratio (total weight 300 mg) and loaded into a silica ampoule in an argon-filled glovebox. The ampoule was subsequently evacuated and flame-sealed. Then it was wrapped with a cocoon of silica wool, placed in a muffle furnace, heated to 500 °C over 10 h, maintained at this temperature for another 10 h, and cooled to room temperature. This procedure yielded shiny brittle gray chunks of As_4Se_4 (Figure S1) which were finely ground using mortar and pestle. The product was not crystalline, with broad amorphous humps observed in the powder X-ray diffraction (PXRD) pattern at the positions expected for the diffraction peaks of the target phase.

Warning

Solvothermal vessels (autoclaves) may develop high autogenic pressures which may result in the release of hot pressurized hazardous ethylenediamine vapors during the reaction. Splashing of the solvent may occur upon opening the autoclaves, causing severe burns. It is highly recommended to wear proper personal protective equipment, such as face-shields, long-sleeve gloves, and tight-cuff lab coats, to place the autoclaves in secondary containment before opening, and to keep furnaces in well-ventilated spaces such as fume hoods.

Synthesis of $Fe_7As_3Se_{12}(en)_6(H_2O)$

$Fe_7As_3Se_{12}(en)_6(H_2O)$ was synthesized by the solvothermal approach under atmospheric conditions. Iron powder (0.4 mmol, <10 microns, Alfa Aesar, 99.5%), selenium powder (0.4 mmol, -100 mesh, Sigma Aldrich, ≥ 99.5%), and the pre-synthesized As_4Se_4 (0.2 mmol) were weighed (total weight ~ 175 mg) with addition of 100 mg of ammonium chloride (Fisher Scientific, 99%). The starting materials were placed in a 23 mL Teflon liner filled with 10 mL of ethylenediamine (filling fraction 43%) which was tightly closed in a stainless-steel autoclave and dwelled at 200 °C in a furnace. After 4 days, the autoclave was taken out of the furnace and naturally cooled to room temperature. The products were filtered and washed with 100% ethanol to obtain a mixture of shiny black needles and shiny orange particles. The latter were washed away by stirring the mixture in ethylenediamine to give a sample composed of black needles only (Figure S2). The orange admixture phase was identified as $[Fe(en)_3]As_2Se_5$ based on the resemblance of it unit cell, found by single crystal X-ray diffraction, to that of $[Mn(en)_3]As_2Se_5$.[37] Formation of this impurity can be prevented by using a higher filling fraction of ethylenediamine (65%) for the reaction, but such reactions resulted in the formation of fine powders of $Fe_7As_3Se_{12}(en)_6(H_2O)$ rather than needle-like crystals.

EDS performed on individual needles gave a composition of heavier elements to be $Fe_{7.2(2)}As_{3.2(1)}Se_{12}$ when normalized to the expected Se content. SEM images showed leftover arsenic that recrystallized into globules (Figure S3). The PXRD pattern of the product washed with en resembled the calculated pattern of $Fe_7As_3Se_{12}(en)_6(H_2O)$ phase but had a significant elemental arsenic peak at $2\theta = 33.4°$ (Figure S4). The As admixture can be minimized by the addition of elemental Se powder into the starting reaction medium. $Fe_7As_3Se_{12}(en)_6(H_2O)$ sample showed good air- and moisture-stability to be stored under ambient conditions for months without oxidation or degradation, as revealed by PXRD. Hand-picked needles from purified samples were used for physical property measurements.

Characterization

$Fe_7As_3Se_{12}(en)_6Cl_2$ was characterized by powder X-ray diffraction (PXRD), single crystal X-ray diffraction, neutron powder diffraction (POWGEN at SNS ORNL), SQUID magnetometry, ^{57}Fe Mössbauer spectroscopy, X-ray absorption spectroscopy (XAS) and X-ray magnetic circular dichroism (XMCD) (ALS ANL), SEM/EDS, and TGA/DSC coupled with IR/MS detection techniques. Heat capacity and resistivity measurements were conducted on a physical property measurement system (PPMS). Density functional theory (DFT) calculations

were conducted using Vienna *ab initio* simulation package (VASP). Further details about the experimental and theoretical methods are provided in the Supporting Information.

Results and Discussion

FT-IR spectroscopy and TGA/DSC

Single crystal X-ray diffraction pointed out the presence of neutral water molecules co-crystallized in the structure. Since it is hard to distinguish H_2O from NH_3/NH_4^+ molecules with X-ray diffraction data, additional characterization measurements were performed to confirm the presence of H_2O molecules in the lattice. FTIR spectrum of $Fe_7As_3Se_{12}(en)_6(H_2O)$ contains a broad signal ~3435 cm^{-1} corresponding to O-H stretching mode and another band ~1630 cm^{-1} corresponding to H-O-H bending modes that indicate the presence of lattice water (Figure S5).[52,53] Absence of a sharp peak at ~1450 cm^{-1} pertaining to N-H stretching vibrations[54] also suggests that the low molecular weight ion/molecule present in the crystal structure is not NH_4^+/ NH_3. To confirm this outcome, TGA/DSC coupled with QMS-FTIR was conducted on $Fe_7As_3Se_{12}(en)_6(H_2O)$, revealing the decomposition of the bulk material above 200 °C with the loss of lattice water molecules (Figure S6). QMS also detected evolution of NH_3 produced by decomposition of carbamate derivatives of ethylenediamine.[55] Gradual degradation of the bulk structure is indicated by the significant FTIR bands corresponding to the ligand ethylenediamine released in 250-275 °C temperature range. With the loss of ethylenediamine, heavy elements combine to form the selenium counterpart of arsenopyrite, FeAsSe, as confirmed by PXRD. Decomposition of the sample placed in an alumina crucible under a constant N_2 flow inside a flow furnace yielded binary $FeSe_2$, ternary FeAsSe, and elemental arsenic around 300 °C. Treatment of the decomposition products in 10 mL ethylenediamine under the same solvothermal conditions does not result in reformation of the parent compound.

Crystal structure

The chiral and polar compound $Fe_7As_3Se_{12}(en)_6(H_2O)$ crystalizes in a monoclinic non-centrosymmetric space group $P2_1$ (No. 4) with the lattice parameters a = 8.7648(6) Å, b = 21.6607(1) Å, c = 12.2894(8) Å, and β = 91.726(2)° (Table S1). The final refined Flack parameter was 0.032(8) for the $P2_1$ space group, confirming the crystal structure to be non-centrosymmetric. In order to further confirm the crystal structure, neutron powder diffraction data were obtained at 100 K and 20 K, which resulted in identical patterns, suggesting the compound does not undergo any structural transition at low temperatures (Figure S7a).

Being neighbors in the Periodic Table, As and Se are hard to distinguish by X-ray diffraction due to similar scattering factors, but they have relatively good contrast in neutron scattering, with coherent scattering lengths of 6.58 fm (As) and 7.97 fm (Se). Rietveld refinement of the neutron diffraction dataset collected at 100 K confirmed the assignments of As and Se sites in the structure solution based on X-ray diffraction data (Figure S7b). Even though X-ray diffraction data suggested two potential water molecules, one fully occupied and the other partially occupied, only the former water molecule was confirmed by the neutron diffraction data. The discrepancy with X-ray data may be due to certain errors in the Fourier density map that occur for light atoms with small X-ray scattering factors.

$Fe_7As_3Se_{12}(en)_6(H_2O)$ consists of $[Fe_5Se_9]$ chains covalently connected by pentagonal $[As_3Se_2]$-Se motifs forming a 2D layered structure. The $[Fe(en)_3]^{2+}$ complexes and H_2O molecules occupy the space between the layers (Figure 1a and 1b). Asymmetric $[As_3Se_2]$-Se rings make the crystal structure polar and chiral. The Fe-As-Se framework is surrounded by Δ-isomers of $[Fe(en)_3]^{2+}$ complexes arranged in channels parallel and perpendicular to the 2D framework. To get a clear picture of the framework and the spacer molecules in the formula unit, the chemical formula can also be written as $[Fe(en)_3]_2[Fe_5Se_9][As_3Se_2]$-Se$(H_2O)$. The space-filling H_2O molecules are located in the vicinity of the pentagonal $[As_3Se_2]$-Se segments (Figure 1b). Fe1 and Fe2 atoms form the octahedral $[Fe(en)_3]^{2+}$ complexes with an average Fe-N bond distance of 2.21(2) Å which is typical for high spin Fe(II) complexes.[56]

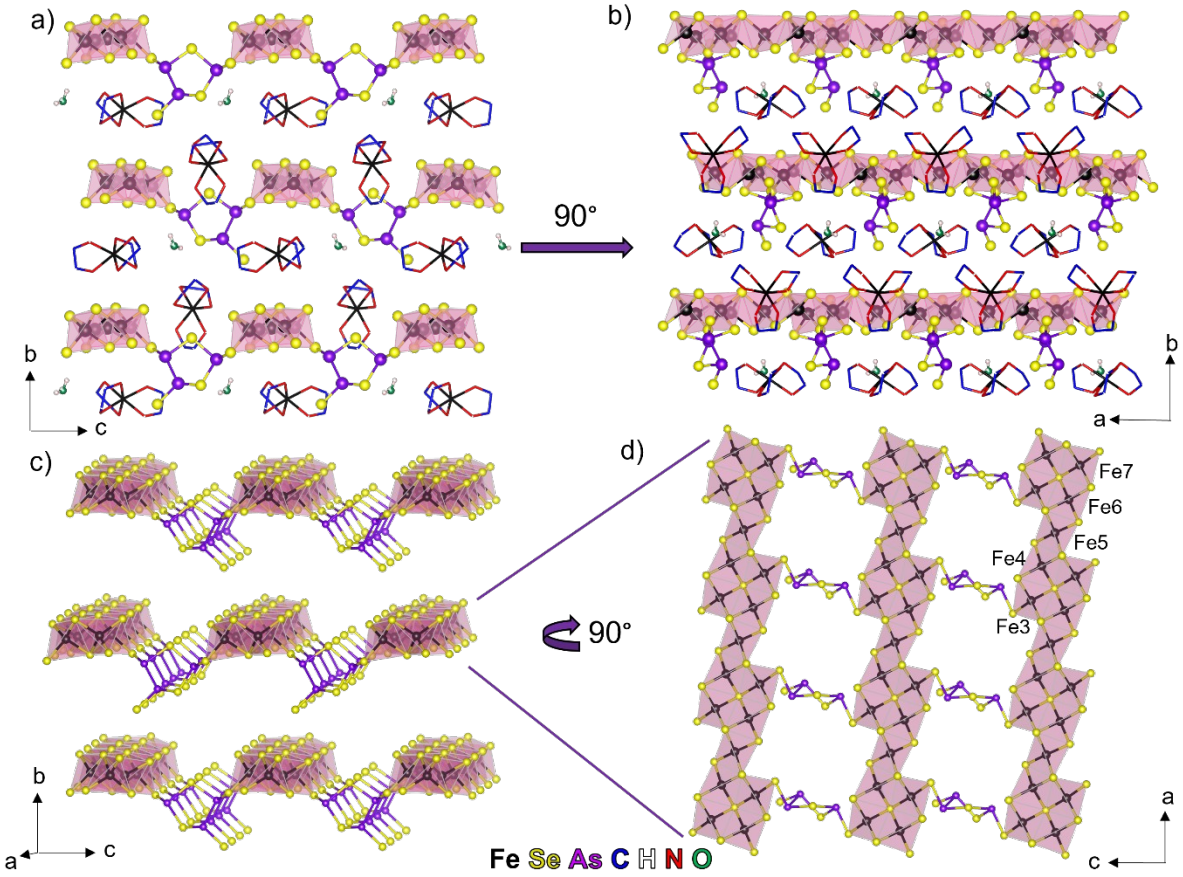

Figure 1. Crystal structure of $Fe_7As_3Se_{12}(en)_6(H_2O)$ = $[Fe(en)_3]_2[Fe_5Se_9][As_3Se_2]$-Se$(H_2O)$. General view along **a)** [100] and **b)** [001] directions. H atoms in *en* are omitted for clarity. **c)** 2D Fe-As-Se framework showing the $[Fe_5Se_9]$ chains connected by $[As_3Se_2]$-Se rings. **d)** Top view of a single Fe-As-Se layer along the [010] direction. Fe: black; Se: yellow; As: purple; N; red; C: blue; O: green.

The 2D Fe-As-Se layers are made up of $[Fe_5Se_9]$ 1D chains interconnected by pentagonal $[As_3Se_2]$ rings with extra terminal Se atoms that swing in between the chains (Figure 1c and 1d). The 2D Fe-As-Se layers are stacked along the [010] direction. $[As_3Se_2]$-Se linkers are

superimposed on one another along the [100] direction with the protruding Se atoms arranged in alternating directionality in adjacent layers (Figure 1c). The top view of a single layer shows each $[Fe_5Se_9]$ chain to be made of diagonally arranged fragments of five $FeSe_4$ edge-sharing tetrahedra labelled as Fe3Fe7 (Figure 1d). Fe3, Fe4, Fe6 and Fe7 tetrahedra share three edges between adjacent fragments giving a double chain appearance, similar to that in AFe_2Se_3 compounds (A = Rb, Cs, Ba).[57–60] In contrast, bridging Fe5 tetrahedra share only two edges within the same fragment. Every fifth tetrahedron of each fragment in one chain is connected to the first tetrahedron of each fragment in the neighboring chain via $[As_3Se_2]$-Se linkers. This gives a ladder appearance to the overall framework. Selenium atoms in the framework exhibit μ_2, μ_3, and μ_4 coordination modes. Some of the μ_2-Se atoms and all the μ_3-Se atoms are located along the edges of the Fe-Se chains while μ_4-Se atoms are at the center of the double-chain part comprised of four tetrahedra (Figure 1d). Remaining μ_2-Se atoms link $[Fe_5Se_9]$ chains to $[As_3Se_2]$-Se rings and, hence, connect to one Fe atom and one As atom. Arsenic atoms in the pentagonal linker have different formal oxidation states. As1, connected to three Se atoms, can be assigned a 3+ oxidation state, while As2 and As3, having two As-Se bonds and one As-As bond, have a 2+ formal oxidation state. The average As-Se distance of 2.39(4) Å and As-As distance of 2.465(1) Å are in line with the sum of As and Se covalent radii, 1.22 Å (As) and 1.17 Å (Se).

The *intra*chain Fe-Fe bond distances vary depending on the position of the corresponding Fe atoms in the $[Fe_5Se_9]$ chains (Table 1). Within the same chain, Fe-Fe bond distances are longer along the *a*-axis than the Fe3–Fe6 and Fe4–Fe7 distances along the *c*-axis. In the compounds with simple single tetrahedral chains, we have found that the Fe-Fe distance correlates with the type of magnetic exchange.[17–19] While distances of 2.87-2.98 Å are typical for antiferromagnetic chains, the shorter Fe-Fe distances of 2.72-2.79 Å result in ferromagnetic nearest-neighbor interactions. The distances observed in the present compound are intermediate between these two ranges. Therefore, we may anticipate a competition between antiferromagnetic and ferromagnetic exchange interactions in the $[Fe_5Se_9]$ chains.

Table 1. Interatomic Fe-Fe distances in the $[Fe_5Se_9]$ chains of $Fe_7As_3Se_{12}(en)_6(H_2O)$.

Pair	Distance (Å)
Fe3–Fe4	2.85(1)
Fe3–Fe6	2.80(1)
Fe4–Fe5	2.84(1)
Fe4–Fe7	2.76(1)
Fe5–Fe6	2.83(1)
Fe6–Fe7	2.86(1)

Assigning the formal oxidation states results in the formula $[(Fe^{2+}(en)_3]_2[(Fe_5)^{13+}(Se^{2-})_{12}](As^{3+})(As^{2+})_2$, which suggests the Fe atoms in the $[Fe_5Se_9]$ chains to be mixed-valent with a net average charge of +2.6. The $FeSe_4$ tetrahedra are far from been

identical, with Fe-Se bond lengths spanning a wide range from 2.329(1) to 2.460(1) Å, giving different tetrahedral volumes (Table 2). Fe5 tetrahedra with only two shared edges have the smallest volume and can be assigned a valence of +3 with certainty. This claim is supported by the calculated bond valence sums (BVS) of Fe^{chain} atoms in previously reported $KFeSe_2$,[61] $Fe_3Se_4(en)_2$,[16] $Fe_3Se_4(en)_3$,[18] $Fe_7Se_8(en)_9Cl_2$,[19] $Fe_3Se_4(dien)_2$,[17] and $Fe_3Se_4(tren)$[17] compounds ranging from +3.0 to + 3.20 whose valence has been confirmed to be +3 by electron count and ^{57}Fe Mössbauer spectroscopy (Table S2). Calculated BVS of Fe^{2+} in $BaFe_2Se_3$ was +2.67.[62] However, mixed-valent compounds such as $Na_3Fe_2Se_4$[63] and $CsFe_2Se_3$[57,64] have BVS of +2.75-3.0 which suggest that Fe3, Fe4, Fe6, and Fe7 atoms in $Fe_7As_3Se_{12}(en)_6(H_2O)$ may have intermediate valence.

Table 2. Tetrahedral volumes and calculated bond valence sums (BVS) of Fe atoms in $[Fe_5Se_9]$ chains of $Fe_7As_3Se_{12}(en)_6(H_2O)$.

Fe atom	**Tetrahedral volume [Å^3]**	**Calculated BVS**
Fe3	7.086	+2.87
Fe4	7.009	+2.96
Fe5	6.757	+3.18
Fe6	6.958	+3.02
Fe7	7.065	+2.92

The effects of the composition and the chemical intercalates on the valence state of Fe atoms can be understood when comparing the Fe-Fe connectivity in some of the 1D and 2D Fe chalcogenides reported to date. Flat fully occupied layers of superconducting FeSe[13] with Fe^{2+} oxidation state gradually transforms into Fe^{3+} with systematic chemical intercalations resulting in cleaving the connectivity between $FeSe_4$ tetrahedra (Figure 2). Fe^{chain} atoms in 1D single chain compounds always acquire a +3 charge ($Fe_7Se_8(en)_9Cl_2$[19], $KFeSe_2$[61]) while those in the 1D compounds with double chains ($Fe_{10}Se_{12}(en)_7$[18], $CsFe_2Se_3$[57]) and 2D compounds with vacancies ($Fe_9S_{10}(en)_{3.5}$[15]) or large voids ($Fe_{18}Se_{21}(en)_{12}Cl_2$[19]) tend to adopt intermediate oxidation states. In $Fe_7As_3Se_{12}(en)_6(H_2O)$, Fe atoms in the 1D $[Fe_5Se_9]$ chains also are mixed-valent as a result of the second type of cations present in the framework.

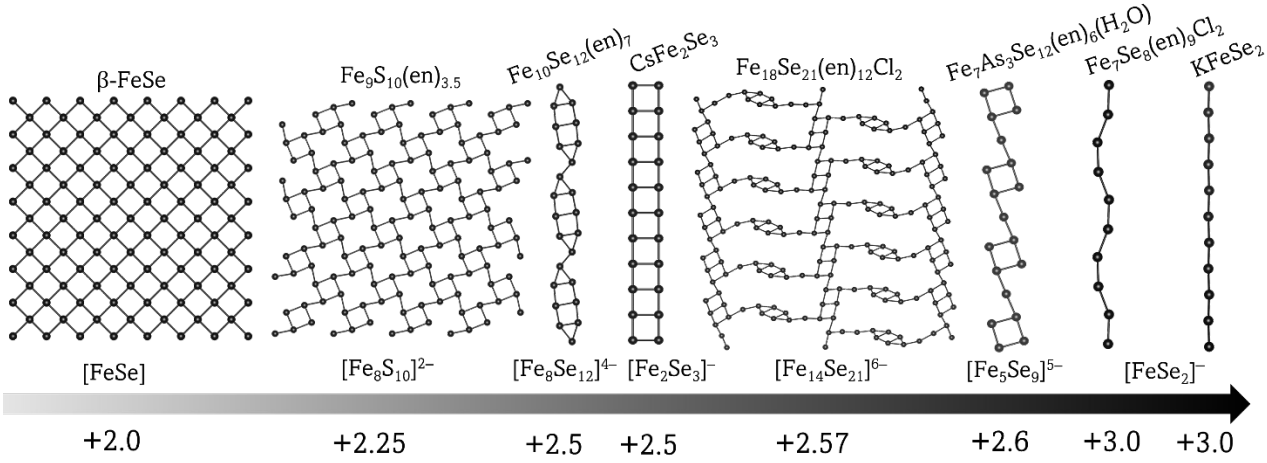

Figure 2. Fe-Fe connectivity in the polyanionic frameworks of 1D and 2D Fe-chalcogenide compounds showcasing the change in the average oxidation state of the Fe atoms. Structural formulae and the polyanionic formulae are given above and below each motif.

X-ray absorption spectroscopy

X-ray absorption spectroscopy (XAS) is an excellent probe for the oxidation state, site symmetry, spin state, and crystal field splitting of Fe ions present in the structure.[65] Fe-$L_{2,3}$ XAS spectra were collected from 300 K to 20 K on a polycrystalline sample mounted on carbon tape glued to Al foil. Before fitting, the spectra were processed for background subtraction and normalized (Figure 3a). At each temperature, the XAS spectrum consists of two doublet structures centered ~708 eV and ~722 eV that correspond to L_3 ($2p_{3/2}$) and L_2 ($2p_{1/2}$) edges respectively.[66] The broad multiplet nature of the peaks is due to the *p-d* and *d-d* Coulomb and exchange interactions.[67] The peak at ~707 eV belongs to the superimposed or combined absorption edges of Fe^{2+} in both octahedral and tetrahedral geometry. Its location is in good agreement with the reported values for O_h Fe^{2+} in $Ba_9Fe_3Se_{15}$[68,69] and T_d Fe^{2+} in FeSe thin films.[70–73] The peak of similar intensity at a higher photon energy of ~709 eV is the main peak of T_d Fe^{3+} L_3 absorption edge occurring in a similar structural environment as in the thiospinel greigite, Fe_3S_4.[74,75]

To analyze the valence of Fe atoms, fittings were performed only on the L_3 absorption edge (Figure 3b, S8) and the count for each valence state was extracted. At 300 K, the Fe^{2+} and Fe^{3+} peaks of the L_3 feature are of comparable intensities which agrees with the ($2Fe_{oct}^{2+}$ + $2Fe_{tetr}^{2+}$): $3Fe_{tetr}^{2+}$ ratio determined by electron counting and Mössbauer spectroscopy (*vide infra*). As the temperature decreases from 250 to 50 K, the lower energy Fe^{2+} peak decreases in intensity and gradually becomes a shoulder to the growing main peak of Fe^{3+} (Figure 3c). The relative concentrations of Fe^{2+} and Fe^{3+} may be slightly inaccurate, since the TEY measurements can be a source of artifacts, such as the saturation in the resonance region that can affect the amplitude of the peaks can effectively change the contributions from different spectral components.

Assuming the Fe^{2+} in the Fe-amine complex does not undergo any valence state change with temperature, the five crystallographically unique Fe atoms in the chains show a clear increase in the spectral contribution from the 3+ state upon cooling (Figure 3d). At 50 K, essentially all Fe atoms in the chains acquire the 3+ valence state. This result confirms the mixed-valent nature of Fe atoms in the anionic chains and, additionally, reveals that the Fe^{2+}/Fe^{3+} ratio is strongly temperature-dependent.

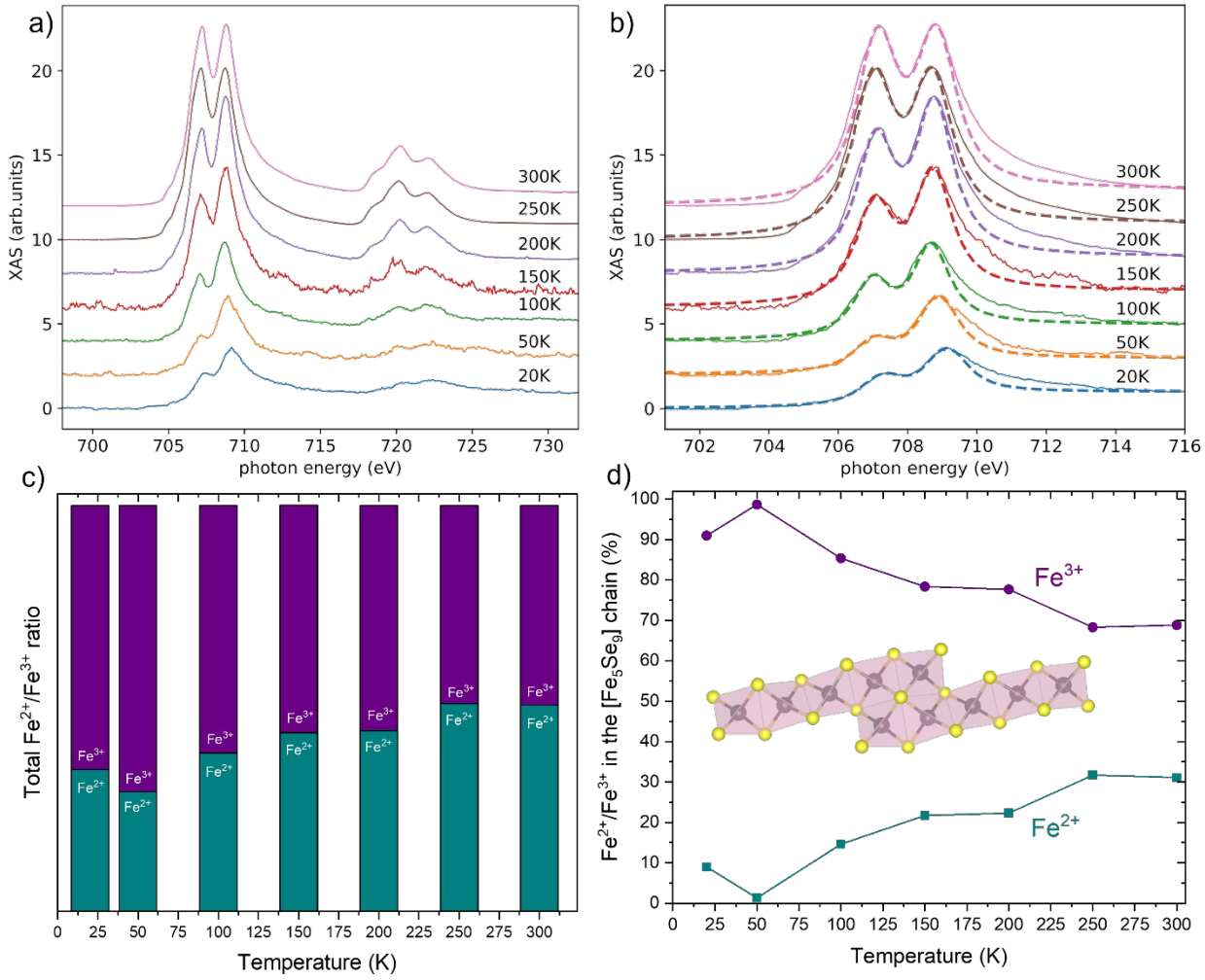

Figure 3. a) XA spectra for $Fe_7As_3Se_{12}(en)_6(H_2O)$ from 20-300 K with the background subtracted and normalized. **b)** Fittings performed on the Fe L_3 absorption region indicated in dashed lines. **c)** Bar graph showing the change in total Fe^{2+}/Fe^{3+} ratio with temperature for all seven Fe atoms in the structure. **d)** Scatter plot showing the change in Fe^{2+}/Fe^{3+} valence count with temperature for the five Fe atoms in the $[Fe_5Se_9]$ chains. For c) and d) Fe^{2+}: cyan; Fe^{3+}: purple.

XMCD spectroscopy

Circular dichroism (CD) is a spectroscopic technique which detects the molecular or solid chirality and reveals important information on different molecular conformations. X-ray magnetic circular dichroism (XMCD) can additionally probe ordered magnetic states due to difference in interaction of spin-up and spin-down electrons with polarized X-rays. In a non-magnetic state, chiral molecules/compounds are capable of interacting with left- and right-polarized electromagnetic radiation and give a non-zero difference signal in the CD measurements.[76] Presence of homochiral metal-ligand complexes, such as Δ- or Λ-$[Fe(en)_3]^{2+}$, can render the entire crystal structure chiral, while presence of both Δ- and λ-isomers related by an inversion center makes the overall structure achiral, as is the case of the majority of hybrid Fe-Se chain compounds.[77] Magnetic and Mössbauer studies discussed below show that the title compound is paramagnetic and not magnetically ordered at room temperature. A prominent XMCD signal observed by the L_3 absorption edge at room temperature, which is much higher than the ordering temperature from Mössbauer spectroscopy, is due to either chiral nature of the compound or field-induced magnetic polarizability of $Fe_7As_3Se_{12}(en)_6(H_2O)$ (Figure 4). Below 200 K, the sample becomes more insulating, as a result, the XMCD signal much weaker as the TEY measurement relies on the conductivity of the sample, hence extracting reliable information becomes rather difficult (Figure S9).

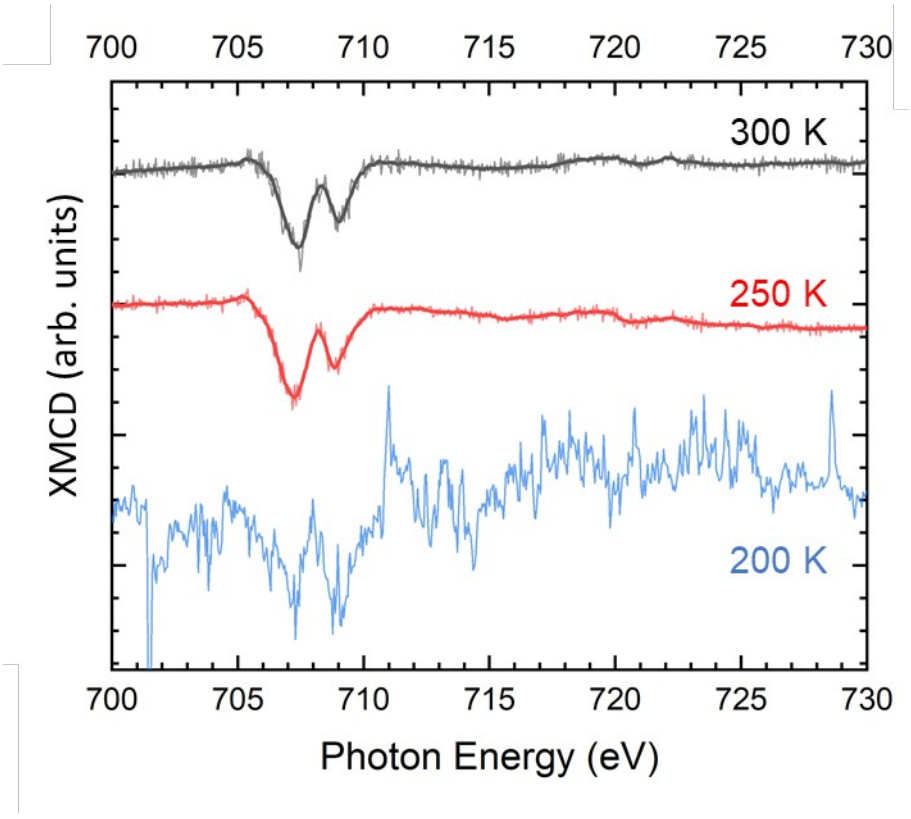

Figure 4. Variable temperature XMCD spectra of $Fe_7As_3Se_{12}(en)_6(H_2O)$ recorded at the Fe *L*-edge under a 3.8 T applied magnetic field.

^{57}Fe Mössbauer spectroscopy

To investigate the oxidation states and magnetic properties of $Fe_7As_3Se_{12}(en)_6(H_2O)$, ^{57}Fe Mössbauer spectroscopy experiments were performed at 6 K, 50 K, 70 K, 100 K, and 293 K (Figures 5, S10). At 293 K, the spectrum does not show any magnetic ordering and can be fitted with three doublets, Q_1, Q_2, and Q_3, which suggest the 2:5 ratio of octahedral to tetrahedral Fe atoms in the crystal structure. The first component, Q_1, with the centroid shift (δ) value of 0.96 mm/s and quadrupole splitting (ΔE_Q) value of 0.70 mm/s represents the octahedral high-spin Fe^{2+} ions of the $[Fe(en)_3]^{2+}$ complexes (Table S3).[78] This finding is consistent with the previously reported room-temperature Mössbauer spectra of $[Fe(en)_3]_3(FeSe_2)_4Cl_2$ that also contains $[Fe(en)_3]^{2+}$ cations.[19] The other components, Q_2 and Q_3, can be attributed to tetrahedrally coordinated Fe atoms in the Fe-As-Se framework. The Q_2 component has δ = 0.36 mm/s and ΔE_Q = 0.67 mm/s while for the Q_3 component has δ = 0.39 mm/s and ΔE_Q = 1.04 mm/s. Both isomer shifts and quadrupole splitting of Q_2 and Q_3 are quite different from those reported for high spin Fe^{3+} in $FeSe_4$ tetrahedra in $[Fe(en)_2](FeSe_2)_2$ (δ = 0.27 mm/s, ΔE_Q = 0.39 mm/s),[16] $[Fe(en)_3]_3(FeSe_2)_4Cl_2$ (δ = 0.26 mm/s, ΔE_Q = 0.35 mm/s),[19] and $RbFeSe_2$ (δ = 0.20 mm/s, ΔE_Q = 0.35 mm/s).[79] Reduction of the Fe oxidation state from 3+ to an intermediate value of (3–*x*) is expected to increase the isomer shift, while the asymmetry of the electron cloud increases the quadrupole splitting. Thus, the observed values of δ and ΔE_Q confirm the intermediate valence of the tetrahedral Fe atoms in the structure of $Fe_7As_3Se_{12}(en)_6(H_2O)$, as discussed above. Moreover, the chains contain two different types of tetrahedral Fe atoms with non-identical oxidation states. Unlike XAS technique, which has an excited state lifetime of ~10^{-15} s, for Mössbauer spectroscopy, the excited state lifetime is ~10^{-9} s, which may lead to unresolved mixed valent peaks when electron fluctuation rate between different Fe sites is faster than the lifetime of the excited state.[80]

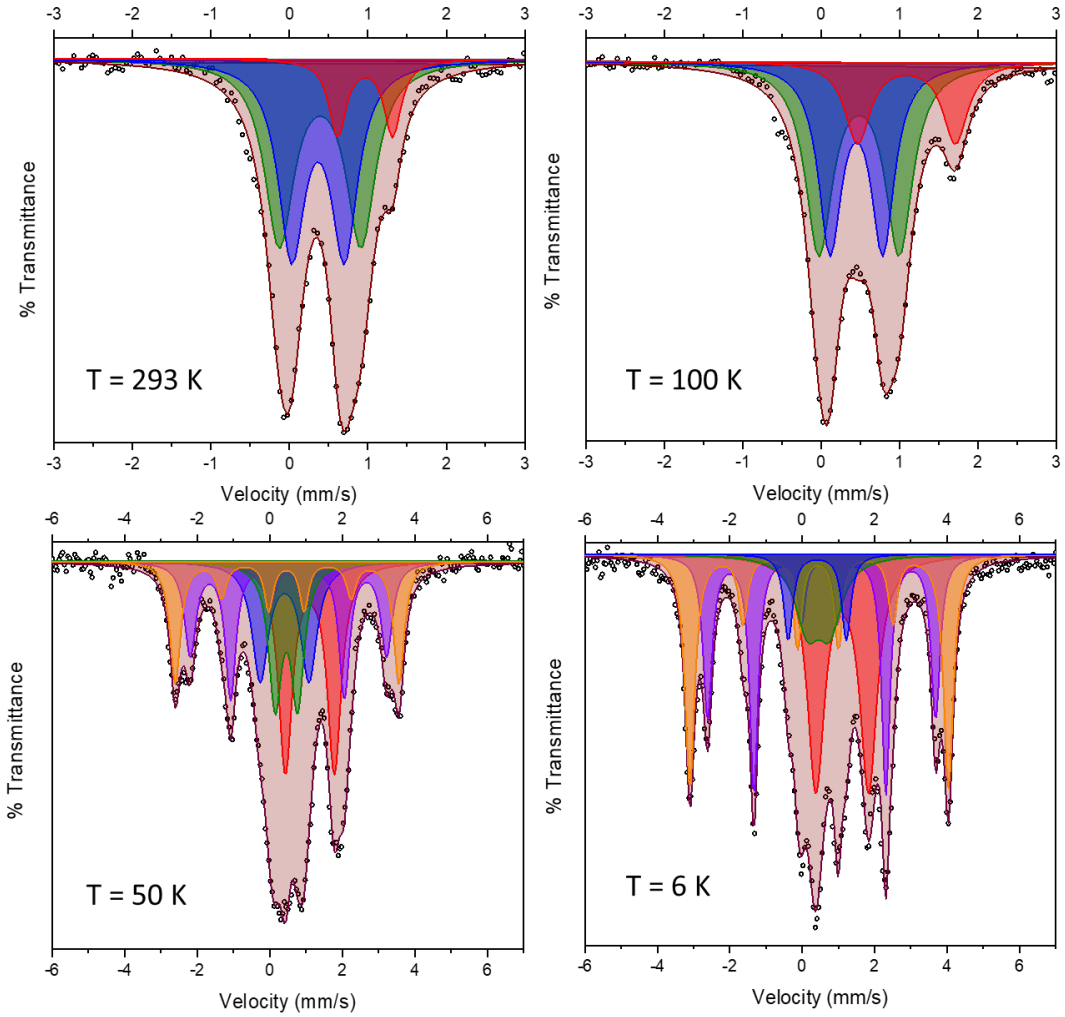

Figure 5. ^{57}Fe Mössbauer spectra for $Fe_7As_3Se_{12}(en)_6(H_2O)$ measured at various temperatures. Experimental: black circles; calculated sum of all contributions: maroon; Q_1: red; Q_2: blue; Q_3: green; Q_{22}: yellow; Q_{33}: purple.

The Mössbauer spectrum recorded at 100 K does not show a substantial difference from the room-temperature spectrum, except for the second-order Doppler effect. There is no sign of magnetically split components. A similar spectrum was observed at 70 K (Figure S10). Both 100 K and 70 K spectra can be fitted with only three non-magnetic doublets. A hyperfine splitting of the Mössbauer signal from the Fe atoms in the chains was observed in the 50 K spectrum, indicating a magnetic ordering event which is subsequently enhanced at 6 K. Fitting these two spectra required five components with similar parameters but different relative intensities. The 50 K spectrum is best fitted with three doublets and two hyperfine sextets (Table S3). The Q_1 component attributed to octahedral Fe^{2+} does not undergo hyperfine splitting. Fe atoms in the $[Fe_5Se_9]$ chains behave differently; signals from 2/5 of Fe atoms (Q_2 and Q_3 components) remain non-magnetic, while the 3/5 signals are magnetically split (Q_{22} and Q_{33} components), indicating

partial magnetic ordering (Figure 6). At 6 K, the octahedral Fe^{2+} signal remains a non-magnetic doublet, while the ratio of magnetic to non-magnetic tetrahedral Fe sites increases from 3:2 to 6:2. The magnetic components show hyperfine splitting values of 22.1 T and 19.5 T. Thus, even at the base temperature the magnetic ordering of tetrahedral Fe atoms is still incomplete.

It is worth mentioning that the intensity of Q_1, which is the signal for high-spin Fe^{2+} increases upon cooling as opposed to Q_2 and Q_3 (Figure 6). It indicates that recoil-free fraction octahedral Fe^{2+} is increasing mush faster than that of tetrahedral Fe^{3+} ions, a similar effect was observed for other hybrid compounds with Fe-Se chains.[19] This trend also applies to the intensities of magnetically split components as well. The decrease in centroid shift values with temperature for Q_1 is caused by second order Doppler effect,[81] while the decrease in ΔE_Q values is due to the temperature-sensitive nature of the electron density distribution over asymmetrically occupied degenerate orbital states of Fe^{2+}.[82]

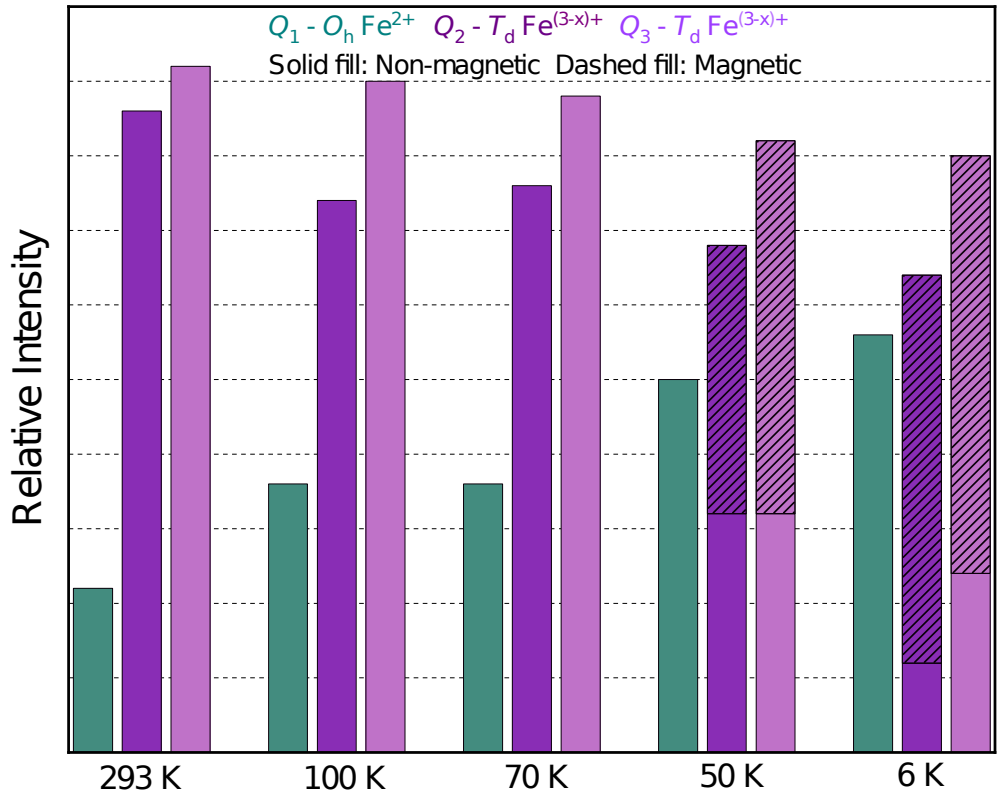

Figure 6. Bar graph comparing the percent intensities of non-magnetic and magnetic components extracted by fitting the Mössbauer spectra for $Fe_7As_3Se_{12}(en)_6(H_2O)$ sample at different temperatures.

To gain more insight into the magnetically ordered phase, neutron powder diffraction measurements were conducted at 100 K and 20 K (Figure S7a). The two patterns did not show significant difference to one another, and no additional magnetic peaks were observed at 20 K. Peaks corresponding to an unidentified trace impurity are clearly visible at low angle at both

temperatures. These peaks are not due to the magnetically ordered phase since they are present in both 100 K and 20 K patterns. The incoherent scattering from hydrogen atoms resulted in moderate pattern quality and high background which may mask the magnetic peaks in the 20 K pattern. Deuteration of the sample may give a lower background but doing this to obtain ~1 g of the sample required for a neutron diffraction experiment is not cost effective.[15]

Electron specific heat

Prior to conducting electronic specific heat measurements on the sample, an Au standard was run to validate instrument. The reported electron heat capacity value for Au is 0.729 mJ/mol·K^2.[83] Linear fit of C_p/T vs T^2 below 20 K^2 using the equation: $C_p/T = \gamma + \beta T^2$, produced a γ coefficient of 0.76(4) mJ/mol·K^2 (Figure S11), which confirmed the reliability of the data measured by the instrument. Electron heat capacity data collected on a pressed pellet of $Fe_7As_3Se_{12}(en)_6(H_2O)$ in H = 0 T and 7 T did not show any peaks below 100 K. At temperatures ~6 K, the two curves crossover (Figures 7a, S12a). The C_p/T dependence on T^2 for 0 T gives a upturn at low temperature which could be attributed to the low-temperature (<2 K) Schottky anomaly due to local AFM interactions.[84,85] This prevents accurate determination of the γ coefficient and Debye temperature. The AFM nature of interactions is supported with suppression (or shifting to even lower temperature) of the anomaly at high applied magnetic field of 7 T (Figures 7b, S12b).

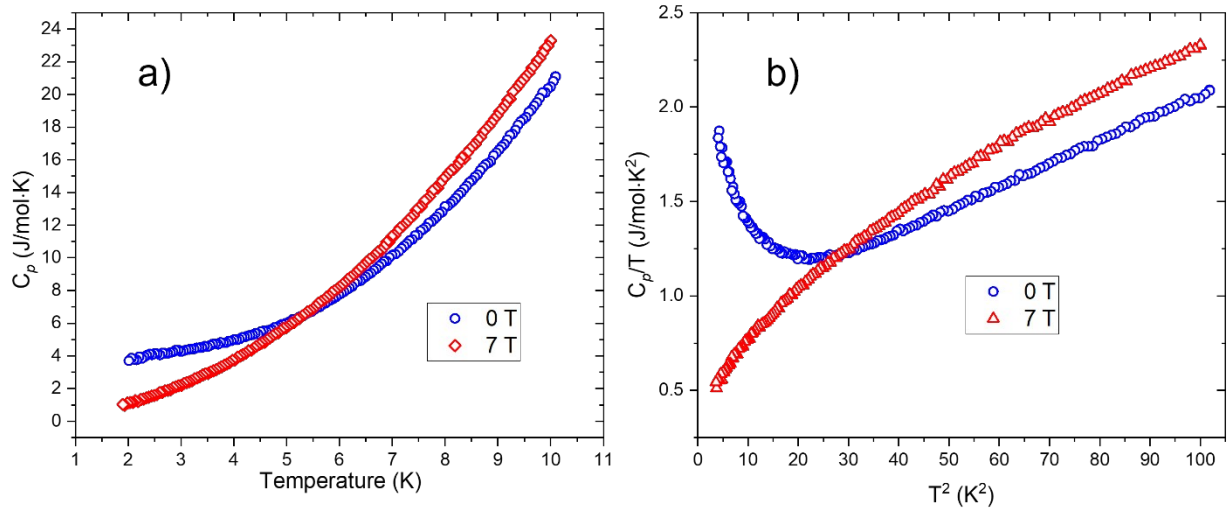

Figure 7. Electron heat capacity data for $Fe_7As_3Se_{12}(en)_6(H_2O)$ conducted in 0 T (blue) and 7 T (red) fields on a pellet pressed under ambient conditions. **a)** Molar specific heat capacity, C_p, as a function of temperature over the range of 2 – 10 K. **b)** C_p/T vs T^2 curve for T^2 < 100 K.

Magnetic measurements

The SQUID magnetic measurements were conducted on finely ground $Fe_7As_3Se_{12}(en)_6(H_2O)$ crystals packed inside a PTFE capsule. A contribution of the empty capsule was subtracted from the raw data to obtain the net moment for the sample. Diamagnetic

correction (χ_D) was applied to the overall calculated susceptibility (χ_{meas}) to account for the intrinsic diamagnetism of all atoms according to the equation $\chi = \chi_{meas} - \chi_D$.[86]

Magnetic susceptibility, χ, measured under an applied field of 1000 Oe, exhibits a typical paramagnetic behavior with no magnetic ordering down to 5 K (Figure 8a, green). A modified Curie-Weiss fit, $\chi = \chi_\circ + C/(T-\theta)$, performed in the 100-350 K range, resulted in the best-fit values for the temperature-independent paramagnetic contribution, $\chi_\circ = 0.0032(1)$ emu/mol, the Curie constant, $C = 4.64(4)$ emu·K/mol, and the asymptotic Curie temperature, $\theta = -9.74(8)$ K ($R^2 = 0.9999$). The latter suggests dominant antiferromagnetic (AFM) nature of the nearest-neighbor interactions in the [Fe_5Se_9] chains. The effective magnetic moment derived from this fit was 6.08 μ_B (2.30 μ_B/Fe). This effective moment is already lower than the expected paramagnetic contribution of two octahedral high-spin $[Fe(en)_3]^{2+}$ complexes, 7.4-7.8 μ_B, thus indicating that the moment of tetrahedral Fe atoms is significantly quenched. The χT curve shows a gradual decrease from 350-75 K, with no anomaly, followed by a substantial drop down to 5 K (Figure 8a, purple). The decrease in the χT product is in line with AFM interactions in the chains.

Isothermal magnetization curves for $Fe_7As_3Se_{12}(en)_6(H_2O)$ are shown in Figure 8b. The lowest values for magnetization are observed at 300 K. As the temperature is lowered, the magnetization gradually increases, reaching the the highest values at 1.8 K. The drastic increase in magnetization observed from 50 – 1.8 K is evident by the maximum moments of 1.4 μ_B/mol = 0.2 μ_B/Fe (50 K) and 4.5 μ_B/mol = 0.64 μ_B/Fe (1.8 K) achieved at the magnetic field of 7 T.

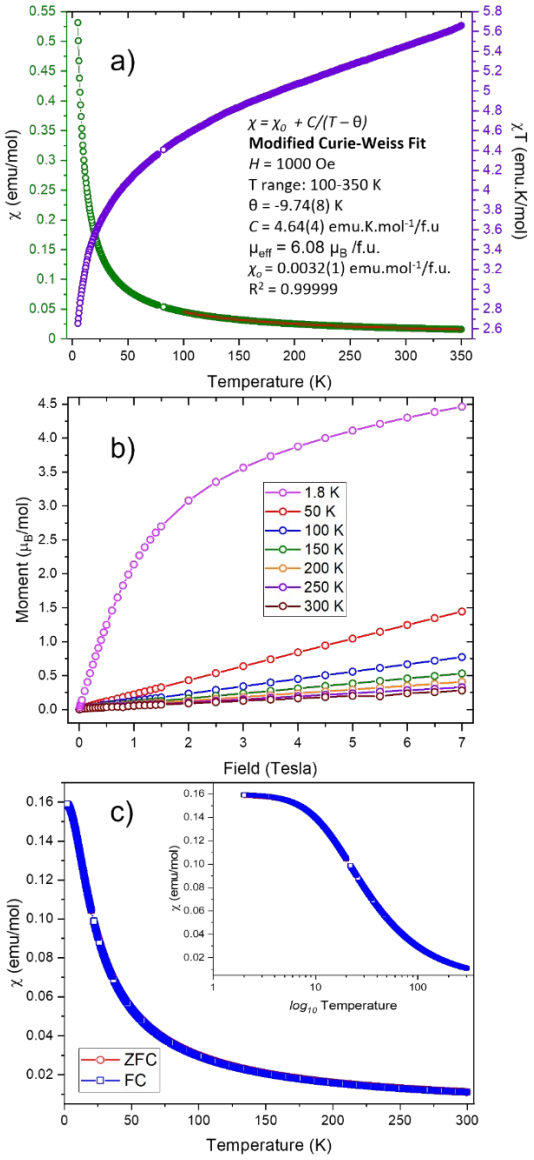

Figure 8. Magnetic properties of $Fe_7As_3Se_{12}(en)_6(H_2O)$: **a)** Temperature dependence of magnetic susceptibility, χ (green circles) and χT (purple circles) measured under an applied field of 1000 Oe. Curie-Weiss fitting for χ vs T plot is shown as a red line. **b)** Isothermal M vs. H curves at 300-1.8 K. **c)** Field-cooled (FC) and zero-field-cooled (ZFC) curves for $Fe_7As_3Se_{12}(en)_6(H_2O)$ measured under an applied field of 7 T. Inset: Same plot with temperature on log scale emphasizing low-temperature part.

The FC and ZFC magnetic susceptibility curves under 25 Oe superimpose on each other and do not display any splitting down to 1.8 K (Figure S14). AC magnetic measurements in the 70-50 K range detected no anomalies that would indicate magnetic ordering or spin-glass formation. One can assume that the hyperfine magnetic splitting detected by Mössbauer spectroscopy stems not from long-range magnetic ordering but from short-range AFM correlations. Under an applied field of 7 T, a clear deflection from the paramagnetic trend is

observed for both ZFC and FC susceptibility data at low temperature, suggesting an onset for long-range ferro- or ferrimagnetic ordering (Figure 8c). We hypothesize that there are competing short range AFM or AFM/FM interactions in the Fe-As-Se 2D layers that prevent long range ordering.

DFT calculations

To probe our hypothesis DFT calculations were performed. The $[Fe(en)_3]^{2+}$ sublattice was replaced by Ba^{2+} ions for the simplicity of calculations keeping the unit cell neutral. The magnetic ground state of the system was explored by calculating the total energy of various magnetic configurations of the Fe-As-Se framework in the unit cell (Z = 2): $Fe_{10}As_6Se_{12}$. The effective *intra*chain and *inter*chain exchange interactions were estimated. The magnetocrystalline anisotropy energy (MAE) was estimated by calculating the total energies of the ground magnetic structure with the spin along different directions. $Fe_{10}As_6Se_{24}$ sublattice consists of two symmetrically equivalent layers. Within a unit cell, each layer contains five Fe atoms that form a pseudo-one-dimensional chain along *a*-direction (Figure 9). Fe3, Fe4, Fe6 and Fe7 atoms form a square on the *ac*-plane; and the Fe5 atom connects with Fe4 and Fe6 atoms, bridging two neighboring four-Fe squares (Table 3 image).

First the magnetic ground state of the pseudo-1D chain was explored considering six different spin configurations (SCs, Table 3). All five ferrimagnetic SCs have lower energies than the ferromagnetic configuration. The SC2, where Fe3-Fe4 and Fe6-Fe7 pairs of the four-Fe square are spin up and the connecting Fe5 being spin down, has the second highest energy. The SC6 configuration with antiparallel pairing of adjacent spins has the lowest energy. Note that this allows AFM pairing of spins between the atoms with shortest interatomic distances, Fe3-Fe6 (2.80 Å) and Fe4-Fe7 (2.76 Å). SCs 4 and 5 with a ferromagnetic component for either Fe3-Fe4 or Fe6-Fe7 have only slightly higher energies <13 meV/Fe than the ground state. The energy differences between these SCs 4, 5, 6 are relatively subtle, suggesting competing *intra*chain FM/AFM magnetic interactions which leads to magnetic frustration. Note that we cannot rule out the possibility of an even lower energy configuration. However, this result implies that the tetrahedral chains are more inclined towards the antiferromagnetic arrangement of spin magnetic moments.

Table 3. The magnetic moments M (μ_B/cell) and total energies E (meV/cell) of various *intra*-chain spin configurations. The numbering of Fe atoms in the chains is as in the fragment shown in the rightmost column.

SCs	Fe3	Fe4	Fe5	Fe6	Fe7	*M* (μ_B/cell)	*E* (meV/cell)	Δ*E* (meV/ Fe)	
1	↑	↑	↑	↑	↑	27.01	0	+295	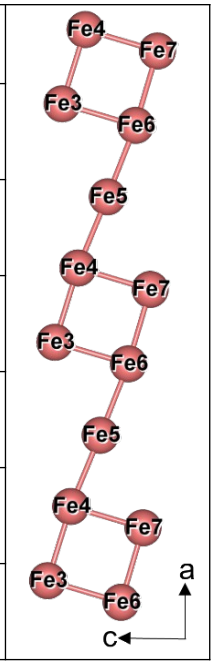
2	↑	↑	↓	↑	↑	16.22	-1750	+120	
3	↑	↓	↓	↓	↑	-4.27	-2240	+71	
4	↓	↓	↑	↓	↑	-5.42	-2820	+13	
5	↑	↓	↑	↓	↓	-5.38	-2890	+6	
6	↑	↓	↑	↓	↑	6.49	-2950	0	

Next, the *inter*chain magnetic interaction was estimated. Starting with the lowest-energy SC6 *intra*-chain configuration and using a 1×1×2 supercell, four SCs with different *inter*chain magnetic ordering were constructed (Figure 9, Table 4). They are ferromagnetic (FM), *C*-type, *G*-type, and *A*-type antiferromagnetic (AFM) SCs, respectively. The *A*-type AFM SC has the lowest energy while the *C*-type SC has the highest energy, suggesting the effective *inter*chain coupling is AFM along *c*-direction but FM along *b*-direction. Note that, comparing Tables 3 and 4, the energy difference between various *inter*chain SCs are generally orders of magnitude smaller than those within different *intra*chain SCs.

Table 4. Magnetization and total energy (with respect to the FM *inter*chain ordering) of SCs with different *inter*chain orderings.

SC	Magnetic moment (μ_B/cell)	Total energy (meV/cell)
FM	6.49	0
C-type AFM	0	2.14
G-type AFM	0	-5.34
A-type AFM	0	-5.81

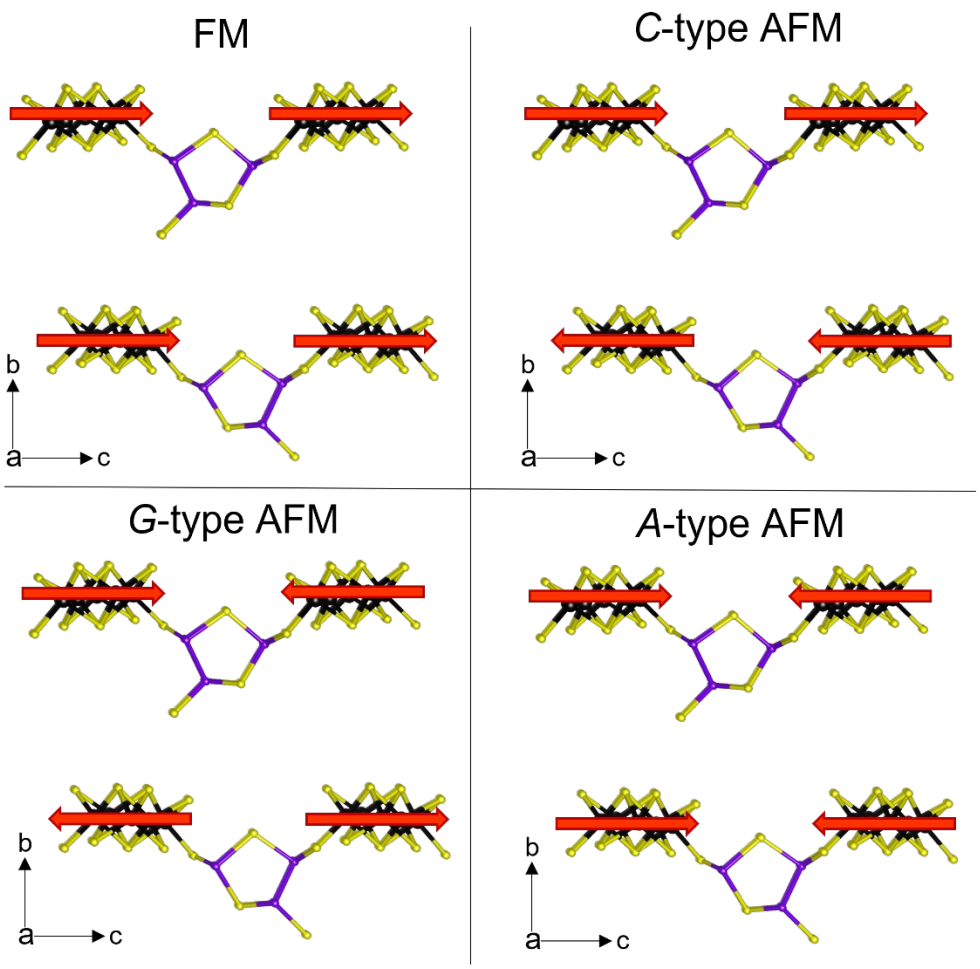

Figure 9. *Inter*chain spin configurations with FM, *C*-type, *G*-type, and *A*-type AFM states. The red arrows represent the direction of Fe magnetic moments on the same type of Fe atoms in different chains. Note that the arrows are indicted along the easy axis +*c* and –*c*. Fe: black; Se: yellow; As: purple.

Magnetocrystalline anisotropy can play a critical role in stabilizing the long-range magnetic ordering in lower-dimensional systems by gaping the spin-wave excitations.[87] Here, MAE was calculated as the total energy difference between different magnetic states in which the magnetization is along the three crystallographic axis directions. The lowest-energy SC6 *intra*-chain structure is employed. We found that, among these three directions, [001] is the easiest direction while [010] is the hardest direction with E[010] – E[001] = 3.495 meV/cell. The [100] direction is slightly harder than [001] with E[010] – E[001] = 0.268 meV/cell.

The DFT calculations shed light on the magnetic interactions in the Fe-As-Se framework. $[Fe_5Se_9]$ chains are composed of mixed valent Fe atoms. The interactions between different types of Fe atoms in the single chains are ferrimagnetic with a competition between several types of the interactions. The valence state of Fe atoms is highly temperature dependent. Upon cooling

the chains became enriched with Fe^{3+} which leads to partial local magnetic ordering at ~50 K. When these chains are connected into a 2D framework, the *inter*chain magnetic interactions favor weaker AFM coupling facilitated by the $[As_3Se_2]$-Se pentagonal linkers. The discrete 2D layers stacked along *b*-axis incline towards FM coupling of moments. However, *inter*chain coupling is much weaker when compared to *intra*chain coupling. Applying of the high magnetic field of 7 T suppresses AFM interactions and favors FM ones, however, this field is still not sufficient to completely transform *intra*chain interactions to be ferromagnetic.

Conclusions

A novel way to induce chirality and polarity in hybrid compounds was demonstrated by using covalent pentagonal As-Se linker. In the resulting chiral Fe_5Se_9 chains Fe atoms have mix-valent oxidation state as evidence by XAS and Mössbauer spectroscopy. Moreover, the Fe oxidation state is temperature dependent. DFT calculations pointed out to competing intrachain and interchain ferrimagnetic interactions which resulted in the hidden local magnetic ordering which was observed by Mössbauer spectroscopy. Research probing the tunability of covalent linkers and their impact on the resulting crystal structure is currently underway.

ASSOCIATED CONTENT

Supporting Information.

Details of synthesis and characterization procedures, crystallographic files, additional X-ray diffraction, neutron diffraction, XAS, XMCD, heat capacity, FTIR, magnetic measurement figures, sample photographs, EDS spectra, SEM images, and bond valence sum table. This material is available free of charge via the Internet at http://pubs.acs.org.

AUTHOR INFORMATION

Corresponding Author

Dr. Kirill Kovnir, kovnir@iastate.edu

Author Contributions

The manuscript was written through contributions of all authors.

Funding Sources

This research was supported by National Science Foundation grants DMR-2003783 to KK and DMR-1905499 to MS. XAS/XMCD experiments of this research used resources of beamline 4.0.2, Advanced Light Source, a U.S. DOE Office of Science User Facility under contract no. DE-AC02-05CH11231. YL and LK were supported by the U.S. Department of Energy, Office of Science, Office of Basic Energy Sciences, Materials Sciences and Engineering Division. Ames Laboratory is operated for the U.S. Department of Energy by Iowa State University under Contract No. DE-AC02-07CH11358. Powder Neutron Diffraction experiment of this research used resources at the POWGEN, BL-11A, Spallation Neutron Source, a DOE Office of Science

User Facility operated by the Oak Ridge National Laboratory. AY acknowledges support from the Carl Trygger Foundation.

Acknowledgements

Our sincere thanks go to the beamline scientists Dr. Qiang Zhang (POWGEN ORNL) for conducting the neutron diffraction experiments and collecting the data. Authors would also like to thank Dr. Warren Straszheim (MARL-ISU) and Dr. Shannon Lee for the help with SEM/EDS data collection and Dr. Brett Boote (CIF-ISU) for his support with FTIR/TGA measurements and analysis.

References

(1) Kamihara, Y.; Hiramatsu, H.; Hirano, M.; Kawamura, R.; Yanagi, H.; Kamiya, T.; Hosono, H. Iron-Based Layered Superconductor: LaOFeP. *J. Amer. Chem. Soc.* **2006**, *128*, 10012–10013.

(2) Kamihara, Y.; Watanabe, T.; Hirano, M.; Hosono, H. Iron-Based Layered Superconductor $La[O_{1-X}F_x]FeAs$ (X= 0.05-0.12) with T_c = 26 K. *J. Amer. Chem. Soc.* **2008**, *130*, 3296–3297.

(3) Mandrus, D.; Sefat, A. S.; McGuire, M. A.; Sales, B. C. Materials Chemistry of $BaFe_2As_2$: A Model Platform for Unconventional Superconductivity. *Chem. Mater.* **2010**, *22*, 715–723.

(4) Meinero, M.; Caglieris, F.; Pallecchi, I.; Lamura, G.; Ishida, S.; Eisaki, H. In-Plane and out-of-Plane Properties of a $BaFe_2As_2$ Single Crystal. *J. Phys. Condens. Matter* **2019**, *31*, 214003.

(5) Ishida, S.; Liang, T.; Nakajima, M.; Kihou, K.; Lee, C. H.; Iyo, A.; Eisaki, H.; Kakeshita, T.; Kida, T.; Hagiwara, M.; Tomioka, Y.; Ito, T.; Uchida, S. Manifestations of Multiple-Carrier Charge Transport in the Magnetostructurally Ordered Phase of $BaFe_2As_2$. *Phys. Rev. B***2011**, *84*, 184514.

(6) Christianson, A. D.; Goremychkin, E. A.; Osborn, R.; Rosenkranz, S.; Lumsden, M. D.; Malliakas, C. D.; Todorov, I. S.; Claus, H.; Chung, D. Y.; Kanatzidis, M. G.; Bewley, R. I.; Guidi, T. Unconventional Superconductivity in $Ba_{0.6}K_{0.4}Fe_2As_2$ from Inelastic Neutron Scattering. *Nature* **2008**, *456*, 930–932.

(7) Rotter, M.; Tegel, M.; Johrendt, D. Superconductivity at 38 K in the Iron Arsenide $(Ba_{1-X}K_x)Fe_2As_2$. *Phys. Rev. Lett.* **2008**, *101*, 4–7.

(8) P Ying, E. T.; Chen, X. L.; Wang, G.; Jin, S. F.; Zhou, T. T.; Lai, X. F.; Zhang, H.; Wang, W. Y. Observation of Superconductivity at 30~46K in $A_xFe_2Se_2$ (A= Li, Na, Ba, Sr, Ca, Yb, and Eu). *Sci. Rep.* **2012**, *2*, 426–432.

(9) Wang, X. C.; Liu, Q. Q.; Lv, Y. X.; Gao, W. B.; Yang, L. X.; Yu, R. C.; Li, F. Y.; Jin, C. Q. The Superconductivity at 18 K in LiFeAs System. *Solid State Commun.* **2008**, *148*, 538–540.

(10) Hsu, F.; Luo, J.; Yeh, K.; Chen, T.; Huang, T.; Wu, P. M.; Lee, Y.; Huang, Y.; Chu, Y.; Yan, D.; Wu, M. Superconductivity in the PbO-Type Structure α-FeSe. *Proc. Natl. Acad. Sci. U. S. A.* **2008**, *05*, 14262–14264.

(11) Huang, F. Observation of Superconductivity in Tetragonal FeS. *J. Amer. Chem. Soc.* **2015**, *137*, 10148–10151.

(12) Fang, M. H.; Pham, H. M.; Qian, B.; Liu, T. J.; Vehstedt, E. K.; Liu, Y.; Spinu, L.; Mao, Z. Q. Superconductivity Close to Magnetic Instability in $Fe(Se_{1-x}Te_x)_{0.82}$. *Phys. Rev. B* **2008**, *78*, 224503.

(13) Greenfield, J. T.; Kamali, S.; Lee, K.; Kovnir, K. A Solution for Solution-Produced β-FeSe: Elucidating and Overcoming Factors That Prevent Superconductivity. *Chem. Mater.* **2015**, *27*, 588–596.

(14) Wu, M.; Rhee, J.; Emge, T. J.; Yao, H.; Cheng, J. H.; Thiagarajan, S.; Croft, M.; Yang, R.; Li, J. A Low Band Gap Iron Sulfide Hybrid Semiconductor with Unique 2D $[Fe_{16}S_{20}]^{8-}$ Layer and Reduced Thermal Conductivity. *Chem. Commun.* **2010**, *46*, 1649–1651.

(15) P. Harmer, C.; Pak, C.; T. Greenfield, J.; N. Adeyemi, A.; H. Gamage, E.; Kovnir, K. Non-Innocent Intercalation of Diamines into Tetragonal FeS Superconductor. *ACS Appl. Energy Mater.* **2021**, *4*, 42–46.

(16) Pak, C.; Kamali, S.; Pham, J.; Lee, K.; Greenfield, J. T.; Kovnir, K. Chemical Excision of Tetrahedral $FeSe_2$ Chains from the Superconductor FeSe: Synthesis, Crystal Structure, and Magnetism of $Fe_3Se_4(en)_2$. *J. Amer. Chem. Soc.* **2013**, *135*, 19111–19114.

(17) Greenfield, J. T.; Pak, C.; Kamali, S.; Lee, K.; Kovnir, K. Control over Connectivity and Magnetism of Tetrahedral $FeSe_2$ Chains through Coordination Fe–Amine Complexes. *Chem. Commun.* **2015**, *51*, 5355–5358.

(18) Stahl, J.; Shlaen, E.; Singer, H.; Johrendt, D. Systematic Dimensional Reduction of the Layered β-FeSe Structure by Solvothermal Synthesis. *Dalt. Trans.* **2018**, *47*, 3264–3271.

(19) Gamage, E. H.; Greenfield, J. T.; Unger, C.; Kamali, S.; K. Clark, J.; Harmer, C. P.; Luo, L.; Wang, J.; Shatruk, M.; Kovnir, K. Tuning Fe–Se Tetrahedral Frameworks by a Combination of $[Fe(en)_3]^{2+}$ Cations and Cl^- Anions. *Inorg. Chem.* **2020**, *59*, 13353–13363.

(20) Zheng, H.; C. Wilfong, B.; Hickox-Young, D.; M. Rondinelli, J.; Y. Zavalij, P.; E. Rodriguez, E. Polar Ferromagnetic Metal by Intercalation of Metal–Amine Complexes. *Chem. Mater.* **2021**, *33*, 4936–4947.

(21) Bode, M.; Heide, M.; Von Bergmann, K.; Ferriani, P.; Heinze, S.; Bihlmayer, G.; Kubetzka, A.; Pietzsch, O.; Blügel, S.; Wiesendanger, R. Chiral Magnetic Order at Surfaces Driven by Inversion Asymmetry. *Nature* **2007**, *447*, 190–193.

(22) Grohol, D.; Matan, K.; Cho, J. H.; Lee, S. H.; Lynn, J. W.; Nocera, D. G.; Lee, Y. S. Spin Chirality on a Two-Dimensional Frustrated Lattice. *Nat. Mater.* **2005**, *4*, 323–328.

(23) Ishikawa, Y.; Tajima, K.; Bloch, D.; Roth, M. Helical Spin Structure in Manganese

Silicide MnSi. *Solid State Commun.* **1976**, *19*, 525–528.

(24) Grigoriev, S. V.; Chernyshov, D.; Dyadkin, V. A.; Dmitriev, V.; Maleyev, S. V.; Moskvin, E. V.; Menzel, D.; Schoenes, J.; Eckerlebe, H. Crystal Handedness and Spin Helix Chirality in $Fe_{1-X}Co_xSi$. *Phys. Rev. Lett.* **2009**, *102*, 037204.

(25) Dzyaloshinsky, I. A Thermodynamic Theory of "Weak" Ferromagnetism of Antiferromagnetics. *J. Phys. Chem. Solids* **1958**, *4*, 241–255.

(26) Moriya, T. Anisotropic Superexchange Interaction and Weak Ferromagnetism. *Phys. Rev.* **1960**, *120*, 91-98.

(27) Taguchi, Y.; Oohara, Y.; Yoshizawa, H.; Nagaosa, N.; Tokura, Y. Spin Chirality, Berry Phase, and Anomalous Hall Effect in a Frustrated Ferromagnet. *Science.* **2001**, *291*, 2573–2576.

(28) Mourigal, M.; Fuhrman, W. T.; Sheckelton, J. P.; Wartelle, A.; Rodriguez-Rivera, J. A.; Abernathy, D. L.; McQueen, T. M.; Broholm, C. L. Molecular Quantum Magnetism in $LiZn_2Mo_3O_8$. *Phys. Rev. Lett.* **2014**, *112*, 027202.

(29) Sheckelton, J. P.; Neilson, J. R.; Soltan, D. G.; McQueen, T. M. Possible Valence-Bond Condensation in the Frustrated Cluster Magnet $LiZn_2Mo_3O_8$. *Nat. Mater.* **2012**, *11*, 493–496.

(30) Sheckelton, J. P.; Foronda, F. R.; Pan, L.; Moir, C.; McDonald, R. D.; Lancaster, T.; Baker, P. J.; Armitage, N. P.; Imai, T.; Blundell, S. J.; McQueen, T. M. Local Magnetism and Spin Correlations in the Geometrically Frustrated Cluster Magnet $LiZn_2Mo_3O_8$. *Phys. Rev. B* **2014**, *89*, 064407.

(31) Sheckelton, J. P.; Neilson, J. R.; McQueen, T. M. Electronic Tunability of the Frustrated Triangular-Lattice Cluster Magnet $LiZn_{2-X}Mo_3O_8$. *Mater. Horizons* **2015**, *2*, 76–80.

(32) Moriya, T.; Miyadai, T. Evidence for the Helical Spin Structure Due to Antisymmetric Exchange Interaction in $Cr_{1/3}NbS_2$. *Solid State Commun.* **1982**, *42*, 209–212.

(33) Sirica, N.; Vilmercati, P.; Bondino, F.; Pis, I.; Nappini, S.; Mo, S. K.; Fedorov, A. V.; Das, P. K.; Vobornik, I.; Fujii, J.; Li, L.; Sapkota, D.; Parker, D. S.; Mandrus, D. G.; Mannella, N. The Nature of Ferromagnetism in the Chiral Helimagnet $Cr_{1/3}NbS_2$. *Commun. Phys.* **2020**, *3*, 65.

(34) Pappas, C. New Twist in Chiral Magnets - A Viewpoint on: Chiral Magnetic Soliton Lattice on a Chiral Helimagnet. *Phys. Rev. Lett* **2012**, *5*, 107202.

(35) Schoo, C.; Bestgen, S.; Egeberg, A.; Seibert, J.; Konchenko, S. N.; Feldmann, C.; Roesky, P. W. Samarium Polyarsenides Derived from Nanoscale Arsenic. *Angew. Chem. Int. Ed.* **2019**, *58*, 4386–4389.

(36) Jiang, H.; Wang, X.; Sheng, T. L.; Hu, S. M.; Fu, R. B.; Wu, X. T. Synthesis, Structure, and Characterization of a Novel Selenidoarsenate: Incorporation of $[Mn(Phen)_2]^{2+}$ Cations into $_\infty{}^1[As^{III}{}_2Se_3(Se_2)]^{2-}$ Chains. *Inorg. Chem. Commun.* **2012**, *17*, 5–8.

(37) Jia, D. X.; Zhao, Q. X.; Dai, J.; Zhang, Y.; Zhu, Q. Y. New Chalcogenidoarsenates with Transition Metal Complex Cations: $[M(en)_3]_2As_2S_5$ (M = Mn, Ni) and $[Mn(en)_3]_2As_2Se_5$. *Z. Anorg. Allg. Chemie* **2006**, *632*, 349–353.

(38) Zell, T.; Shi, W.; Langer, R.; Ponikiewski, L.; Rothenberger, A. Reactivity of a Heterocyclic As–Se Compound with Metal Salts: Syntheses and Structures of the First Copper Complexes and of New Alkali Metal Salts Containing As–Se Anions. *J. Chem. Soc. Dalt. Trans.* **2007**, 932–937.

(39) Zhao, J.; Liang, J.; Pan, Y.; Zhang, Y.; Jia, D. New Polyselenidoarsenate Salts with Transition Metal Complexes as Counterions: Solvothermal Synthesis, Crystal Structures, and Properties of $[M(dien)_2]As_2Se_6$ (M = Co, Ni) and $[Mn(dap)_3]As_2Se_6$. *Monat. Chem.* **2011**, *142*, 1203–1209.

(40) Chen, R.; Tang, W.; Jiang, W.; Zhang, Y.; Jia, D. Solvent Effect on Condensation of Pyramidal $[AsSe_3]^{3-}$: Solvothermal Syntheses of New Selenidoarsenates Containing Transition Metal(II) Complexes with 1,10-Phenanthroline. *J. Coord. Chem.* **2012**, *65*, 3316–3328.

(41) Fu, M. L.; Guo, G. C.; Liu, X.; Liu, B.; Cai, L. Z.; Huang, J. S. Syntheses, Structures and Properties of Three Selenoarsenates Templated by Transition Metal Complexes. *Inorg. Chem. Commun.* **2005**, *8*, 18–21.

(42) Dimaio, A. J.; Rheingold, A. L. Structural Chemistry of Transition-Metal Complexes Containing Arsenic-Arsenic Bonds. *Chem. Rev.* **1990**, *90*, 169–190.

(43) Kromm, A.; Almsick, V. T.; Sheldrick, W. S. Solvothermal Synthesis and Structure of Chalcogenidoarsenate Anions. *Z. Naturforsch. B* **2010**, *65*, 918–936.

(44) Kromm, A.; Sheldrick, W. S. Manganese(II) Complexes with Bridging Selenidoarsenate(III) Anions $[AsSe_2(Se_2)]^{3-}$ and $[(AsSe_2)_2(\mu\text{-}Se_2)]^{4-}$. *Z. Anorg. Allg. Chemie* **2009**, *635*, 205–207.

(45) Kromm, A.; Sheldrick, W. S. (Terpyridine)Manganese(II) Coordination Polymers with Thio- and Selenidoarsenate(III) Ligands: Coligand Influence on the Chalcogenidoarsenate(III) Species and Coordination Mode. *Z. Anorg. Allg. Chemie* **2008**, *634*, 2948–2953.

(46) Belin, C. H. E.; Charbonnel, M. M. Heteroatomic Polyanions of Post Transition Elements. Synthesis and Structure of a Salt Containing the Diarsenichexaselenate(2-) Anion, $As_2Se_6^{2-}$. *Inorg. Chem.* **1982**, *21*, 2504–2506.

(47) Blacque, O.; Brunner, H.; Kubicki, M. M.; Leis, F.; Lucas, D.; Mugnier, Y.; Nuber, B.; Wachter, J. Structural Rearrangements in Triple-Decker-like Complexes with Mixed Group 15/16 Ligands: Synthesis and Characterization of the Redox Couple $[Cp_2{*}Fe_2As_2Se_2]/[Cp_2{*}Fe_2As_2Se_2]^+$ ($Cp^*=C_5Me_5$). *Chem. Eur. J.* **2001**, *7*, 1342–1349.

(48) Ansari, M. A.; Ibers, J. A.; C.O'Neal, S.; Pennington, W. T.; Kolis, J. W. Solution Chemistry of Arsenic Selenides: Synthesis, Spectroscopy and the X-Ray Structures of

$[PPh_4]_2[As_nSe_6]$, n = 2,4. *Polyhedron* **1992**, *11*, 1877–1881.

(49) Drake, G. W.; Kolis, J. W. The Chemistry of Mixed 15/16 Main Group Clusters. *Coord. Chem. Rev.* **1994**, *137*, 131–178.

(50) Smith, D. M.; Pell, M. A.; Ibers, J. A. Se_2^{2-}, Se_5^{2-}, and Se_7^{2-} Ligands in $[NEt_4]_2[As_2Se_6]$, [enH][$AsSe_6$].2.2.2-cryptand, $[NEt_4][AsSe_8]$, and $[(en)_2In(SeAs(Se)Se_2)]$,en. *Inorg. Chem* **1998**, *37*, 2340–2343.

(51) Smith, D. M.; Park, C.-W.; Ibers, J. A. Preparation and Structures of the 2.2.2-Cryptand(1+) Salts of the $[Sb_2Se_4]^{2-}$, $[As_2S_4]^{2-}$, $[As_{10}S_3]^{2-}$, and $[As_4Se_6]^{2-}$ Anions. *Inorg. Chem* **1996**, *35*, 6682–6687.

(52) Cheng, F.; Cao, Q.; Guan, Y.; Cheng, H.; Wang, X.; Miller, J. D. FTIR Analysis of Water Structure and Its Influence on the Flotation of Arcanite (K_2SO_4) and Epsomite ($MgSO_4 \cdot 7H_2O$). *Int. J. Miner. Process.* **2013**, *122*, 36–42.

(53) Falk, M.; Huang, C.-H.; Knop, O. Infrared Studies of Water in Crystalline Hydrates: Location of Hydrogen Atoms and Evidence for a Bifurcated Hydrogen Bond in $K_2SnCl_4 \bullet H_2O$. *Can. J. Chem.* **1974**, *52*, 2380–2388.

(54) Max, J. J.; Chapados, C. Aqueous Ammonia and Ammonium Chloride Hydrates: Principal Infrared Spectra. *J. Mol. Struct.* **2013**, *1046*, 124–135.

(55) Jackson, P.; Fisher, K. J.; Attalla, M. I. Tandem Mass Spectrometry Measurement of the Collision Products of Carbamate Anions Derived from CO_2 Capture Sorbents: Paving the Way for Accurate Quantitation. *J. Am. Soc. Mass Spectrom.* **2011**, *22*, 1420–1431.

(56) Konig, E.; Watson, K. J. The Fe-N Bond Lengths, The "Ionic Radii" of Iron (II), and the Crystal Field Parameters (10Dq) in a High-Spin and Low-Spin [Fe^{II}-N_6] Complex. *Chem. Phys. Lett.* **1970**, *6*, 5–7.

(57) Klepp, K. O.; Sparlinek, W.; Boiler, H. Mixed Valent Ternary Iron Chalcogenides : AFe_2X_3 (A = Rb , Cs ; X = Se , Te). *J. Alloy. Compd.* **1996**, *238*, 1–5.

(58) Lei, H.; Ryu, H.; Frenkel, A. I.; Petrovic, C. Anisotropy in $BaFe_2Se_3$ Single Crystals with Double Chains of FeSe Tetrahedra. *Phys. Rev. B* **2011**, *84*, 214511.

(59) Nambu, Y.; Ohgushi, K.; Suzuki, S.; Du, F.; Avdeev, M.; Uwatoko, Y.; Munakata, K.; Fukazawa, H.; Chi, S.; Ueda, Y.; Sato, T. J. Block Magnetism Coupled with Local Distortion in the Iron-Based Spin-Ladder Compound $BaFe_2Se_3$. *Phys. Rev. B* **2012**, *85*, 64413.

(60) Du, F.; Ohgushi, K.; Nambu, Y.; Kawakami, T.; Avdeev, M.; Hirata, Y.; Watanabe, Y.; Sato, T. J.; Ueda, Y. Stripelike Magnetism in a Mixed-Valence Insulating State of the Fe-Based Ladder Compound $CsFe_2Se_3$. *Phys. Rev. B* **2012**, *85*, 214436.

(61) Bronger, W.; Kyas, A.; Müller, P. The Antiferromagnetic Structures of $KFeS_2$, $RbFeS_2$, $KFeSe_2$, and $RbFeSe_2$ and the Correlation between Magnetic Moments and Crystal Field Calculations. *J. Solid State Chem.* **1987**, *70*, 262–270.

(62) Caron, J. M.; Neilson, J. R.; Miller, D. C.; Llobet, A.; McQueen, T. M. Iron Displacements and Magnetoelastic Coupling in the Antiferromagnetic Spin-Ladder Compound $BaFe_2Se_3$. *Phys. Rev. B* **2011**, *84*, 180409(R).

(63) Ensling, J.; Gütlich, P.; Spiering, H.; Klepp, K. Mössbauer and Magnetic Studies of Mixed-Valence Linear Chain Compounds: $Na_3Fe_2S_4$ and $Na_3Fe_2Se_4$. *Hyperf. Inter.* **1986**, 599–601.

(64) Du, F.; Ohgushi, K.; Nambu, Y.; Kawakami, T.; Avdeev, M.; Hirata, Y.; Watanabe, Y.; Sato, T. J.; Ueda, Y. Stripelike Magnetism in a Mixed-Valence Insulating State of the Fe-Based Ladder Compound $CsFe_2Se_3$. *Phys. Rev. B* **2012**, *85*, 214436.

(65) Pearce, C. I.; Pattrick, R. A. D.; Vaughan, D. J. Electrical and Magnetic Properties of Sulfides. *Rev. Mineral. Geochem.* **2006**, *61*, 127–180.

(66) Kuiper, P.; Searle, B. G.; Rudolf, P.; Tjeng, L. H.; Chen, C. T. X-Ray Magnetic Dichroism of Antiferromagnet Fe_2O_3: The Orientation of Magnetic Moments Observed by Fe 2*p* X-ray Absorption Spectroscopy. *Phys. Rev. Lett.* **1993**, *70*, 1549–1552.

(67) Van Der Laan, G.; Kirkman, I. W. The 2*p* Absorption Spectra of 3*d* Transition Metal Compounds in Tetrahedral and Octahedral Symmetry. *J. Phys. Condens. Matter* **1992**, *4*, 418–204.

(68) Zhang, J.; Duan, L.; Wang, Z.; Wang, X.; Zhao, J.; Jin, M.; Li, W.; Zhang, C.; Cao, L.; Deng, Z.; Hu, Z.; Agrestini, S.; Valvidares, M.; Lin, H.; Chen, C.; Zhu, J.; Jin, C. The Synthesis of a Quasi-One-Dimensional Iron-Based Telluride with Antiferromagnetic Chains and a Spin Glass State. *Inorg. Chem.* **2020**, *59*, 5377–5385.

(69) Zhang, J.; Komarek, A. C.; Jin, M.; Wang, X.; Jia, Y.; Zhao, J.; Li, W.; Hu, Z.; Peng, W.; Wang, X.; Tjeng, L. H.; Deng, Z.; Yu, R.; Feng, S.; Zhang, S.; Liu, M.; Yang, Y.; Lin, H.; Chen, C.; Li, X.; Zhu, J.; Jin, C. High-Pressure Synthesis, Crystal Structure, and Properties of Iron-Based Spin-Chain Compound $Ba_9Fe_3Se_{15}$. *Phys. Rev. Mater.* **2021**, *5*, 054606.

(70) Pereira, V. M.; Wu, C. N.; Liu, C. E.; Liao, S.-C.; Chang, C. F.; Kuo, C.-Y.; Koz, C.; Schwarz, U.; Lin, H.-J.; Chen, C. T.; Tjeng, L. H.; Altendorf, S. G. Molecular Beam Epitaxy Preparation and in Situ Characterization of FeTe Thin Films. *Phys. Rev. Mater.* **2020**, *4*, 023405.

(71) Chen, T. K.; Luo, J. Y.; Ke, C. T.; Chang, H. H.; Huang, T. W.; Yeh, K. W.; Chang, C. C.; Hsu, P. C.; Wu, C. Te; Wang, M. J.; Wu, M. K. Low-Temperature Fabrication of Superconducting FeSe Thin Films by Pulsed Laser Deposition. *Thin Solid Films* **2010**, *519*, 1540–1545.

(72) Tsukada, A.; Luna, K. E.; Hammond, R. H.; Beasley, M. R.; Zhao, J. F.; Risbud, S. H. Pulsed Laser Deposition Conditions and Superconductivity of FeSe Thin Films. *Appl Phys A* **2011**, *104*, 311–318.

(73) Telesca, D.; Nie, Y.; Budnick, J. I.; Wells, B. O.; Sinkovic, B. Impact of Valence States

on the Superconductivity of Iron Telluride and Iron Selenide Films with Incorporated Oxygen. *Phys. Rev. B* **2012**, *85*, 214517.

(74) Chang, L.; Pattrick, R. A. D.; Laan, G. van der; Coker, V. S.; Roberts, A. P. Enigmatic X-ray Magnetic Circular Dichroism in Greigite (Fe_3S_4). *Can. Mineral.* **2012**, *50*, 667–674.

(75) Pattrick, R. A. D.; Coker, V. S.; Akhtar, M.; Malik, M. A.; Lewis, E.; Haigh, S.; O'Brien, P.; Shafer, P. C.; Laan, G. van der. Magnetic Spectroscopy of Nanoparticulate Greigite, Fe_3S_4. *Mineral. Mag.* **2017**, *81*, 857–872.

(76) Zhang, Y.; Rouxel, J. R.; Autschbach, J.; Govind, N.; Mukamel, S. X-ray Circular Dichroism Signals: A Unique Probe of Local Molecular Chirality. *Chem. Sci.* **2017**, *8*, 5969–5978.

(77) Chamayou, A. C.; Lüdeke, S.; Brecht, V.; Freedman, T. B.; Nafie, L. A.; Janiak, C. Chirality and Diastereoselection of Δ/∇-Configured Tetrahedral Zinc Complexes through Enantiopure Schiff Base Complexes: Combined Vibrational Circular Dichroism, Density Functional Theory, ^{1}H NMR, and X-ray Structural Studies. *Inorg. Chem.* **2011**, *50*, 11363–11374.

(78) Kamali-M., S.; Ericsson, T.; Wäppling, R. Characterization of Iron Oxide Nanoparticles by Mössbauer Spectroscopy. *Thin Solid Films* **2006**, *515* (2 SPEC. ISS.), 721–723.

(79) Seidov, Z.; Krug Von Nidda, H.-A.; Tsurkan, V.; Filippova, I. G.; Günther, A.; Gavrilova, T. P.; Vagizov, F. G.; Kiiamov, A. G.; Tagirov, L. R.; Loidl, A. Magnetic Properties of the Covalent Chain Antiferromagnet $RbFeSe_2$. *Phys. Rev. B* **2016**, *94*, 134414.

(80) Kovnir, K.; Reiff, W. M.; Menushenkov, A. P.; Yaroslavtsev, A. A.; Chernikov, R. V; Shatruk, M. "Chemical Metamagnetism": From Antiferromagnetic $PrCo_2P_2$ to Ferromagnetic $Pr_{0.8}Eu_{0.2}Co_2P_2$ via Chemical Compression. *Chem. Mater* **2011**, *23*, 3021–3024.

(81) Umemura, Y.; Minai, Y.; Tominaga, T. Structural Distortion of 6-Coordinated Fe(II) Complexes in Zeolite Y. *J. Phys. Chem. B* **1999**, *103*, 647–652.

(82) Brozek, C. K.; Ozarowski, A.; Stoian, S. A.; Dincă, M. Dynamic Structural Flexibility of Fe-MOF-5 Evidenced by ^{57}Fe Mössbauer Spectroscopy. *Inorg. Chem. Front.* **2017**, *4*, 782–788.

(83) Kittel, C. *Introduction to Solid State Physics*, 8th Editio.; Johnson, S., McFadden, P., Eds.; John Wiley & Sons, Inc: New York, NY, **2004**.

(84) Collocott, S. J.; Driver, R.; Dale, L.; Dou, S. X. Schottky Anomaly in the Heat Capacity of the High-Tc Superconductor $YBa_zCu_30_7$. *Phys. Rev. B* **1988**, *37*, 7917.

(85) Adhikari, R. B.; Shen, P.; Kunwar, D. L.; Jeon, I.; Maple, M. B.; Dzero, M.; Almasan, C. C. Magnetic Field Dependence of the Schottky Anomaly in Filled Skutterudites $Pr_{1-x}Eu_xPt_4Ge_{12}$. *Phys. Rev. B* **2019**, *100*, 174509.

(86) Bain, G. A.; Berry, J. F. Diamagnetic Corrections and Pascal's Constants. *J. Chem. Educ.*

2008, *85*, 532–536.

(87) Mkhitaryan, V. V; Ke, L. Self-Consistently Renormalized Spin-Wave Theory of Layered Ferromagnets on the Honeycomb Lattice. *Phys. Rev. B* **2021**, *104*, 64435.

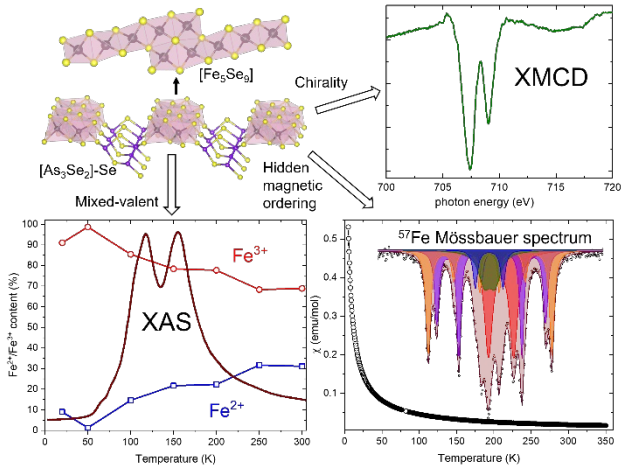
[Fe5Se9]
[As3Se2]-Se
Chirality
Hidden
magnetic
ordering
Mixed-valent
XMCD
photon energy (eV)
XAS
Fe3+
Fe2+
Fe2+/Fe3+ content (%)
Temperature (K)
57Fe Mössbauer spectrum
χ (emu/mol)
Temperature (K)